Mechanisms of the paraelectric to ferroelectric phase transition in RbH_2PO_4 probed by purely resonant x-ray diffraction

C. Richter,[1,4] D. V. Novikov,[1,*] E. Kh. Mukhamedzhanov,[3] M. M. Borisov,[3] K. A. Akimova,[2] E. N. Ovchinnikova,[2] A. P. Oreshko,[2] J. Strempfer,[1] M. Zschornak,[4] E. Mehner,[4] D. C. Meyer,[4] and V. E. Dmitrienko[5]

[1]*Deutsches Elektronen-Synchrotron, DESY, Photon Science, Hamburg, Germany*

[2]*Physical Department of Moscow State University, Moscow, Russia*

[3]*RRC "Kurtchatov Institute," Moscow, Russia*

[4]*Institut für Experimentelle Physik, TU Bergakademie Freiberg, Freiberg, Germany*

[5]*A.V. Shubnikov Institute of Crystallography, Moscow, Russia*

(Received 18 December 2013; revised manuscript received 25 February 2014; published 27 March 2014)

Resonant x-ray diffraction was used to study the proton jumps in hydrogen-bonded rubidium dihydrogen phosphate (RDP) crystals. In the paraelectric RDP phase, hydrogen is delocalized between two crystallographically equivalent positions. At lower temperatures, this symmetry can be broken, which defines the processes that lead to the para- to ferroelectric phase transition. We have measured the energy spectra of the forbidden reflections 006 and 550 at incident radiation energies close to the Rb K edge in a wide temperature range, down to the temperature of the ferroelectric phase transition. In the paraelectric phase, we observed a growth of integrated intensity for both forbidden reflections with temperature. This behavior is opposite to conventional nonresonant Bragg reflections, where intensity decreases in accordance with the Debye-Waller factor. The developed theoretical model explains this effect with the thermal motion induced (TMI) scattering mechanism and also confirms the adiabatic approximation stating that electrons instantly follow the nuclei movements. In the 550 energy spectra, we have observed an additional contribution to the resonant structure factor, which could be associated with the presence of transient Slater-type proton configurations (PC) in the half-filled hydrogen position.

DOI: 10.1103/PhysRevB.89.094110 PACS number(s): 61.05.cp, 61.05.cj, 78.70.Ck, 78.70.Dm

I. INTRODUCTION

Rubidium dihydrogen phosphate (RDP) belongs to the family of the hydrogen-bonded crystals and is isomorphous to its best-known representative potassium dihydrogen phosphate (KDP) [1]. When cooling below 146 K, RDP undergoes a structural transformation from the paraelectric ($I\bar{4}2d$) to the ferroelectric phase ($Fdd2$) [2–4]. Another phase transition from tetragonal to monoclinic phase at about 90 °C is described in literature [5–8].

The nature of the phase transitions in crystals of KDP family is a subject of many years of discussions [9–16]. Usually, it is associated with hydrogen ordering and rotations of PO_4 groups. The static and dynamic properties of these systems are described on the basis of the configuration energy determined by proton configurations. In both theoretical and experimental work, the type of proton transfer between two sites has been discussed. A tunneling of protons in KDP between the two positions in a double-well potential was proposed by Blinc [11] and further confirmed experimentally [13].

Whilst the crystal structures of RbH_2PO_4 and KH_2PO_4 are closely similar, some small but important differences were revealed [4]. In particular, the separation of the disordered proton sites in the tetragonal phase is significantly larger in RbH_2PO_4 (by −0.05 Å), yet the hydrogen bond lengths differ by only 0.003 Å and the transition temperatures by only 23 K. The crystal structure of RDP below the phase transition temperature has been presumed to be isomorphous with that of orthorhombic KDP, but the transition to be much less abrupt in RDP.

Resonant x-ray diffraction has been developed as a method to study structural, magnetic, and electronic properties of crystals [17–24]. Synchrotron sources allow to study the energy spectra and polarization properties of Bragg reflections. When the conventional part of x-ray scattering is absent, reflections still can appear at incident radiation energies close to absorption edges due to the anisotropy in resonant scattering [25–28]. These "forbidden" reflections provide the possibility to study small contributions to the atomic scattering factor caused by various multipole transitions or displacements of the atoms from their average sites [29–33]. Even slight atomic displacements due to thermal vibrations influence the resonant atomic scattering factor resulting in the so-called thermal motion induced (TMI) scattering contribution, which was successfully observed in Ge [34,35], ZnO, and GaN [36,37]. Its main feature is the growth of the integrated intensity with temperature in contrast to conventional Bragg reflections, whose intensity decreases with temperature according to the Debye-Waller factor. An additional contribution to the resonant scattering factor caused by point defects has been predicted [33], but not yet observed experimentally.

In crystals of the KDP family, hydrogen atoms fill only half of the crystallographic position. Being distributed randomly, the symmetry of proton configurations may be lower than that of the crystal and can be accompanied by relaxation of the neighboring atoms. Taking into account the displacement of the resonant atom, an additional contribution to the resonant atomic factor can appear [38]. In the present paper, the temperature dependence of two forbidden reflections in RDP was studied experimentally and described theoretically.

*Corresponding author: dmitri.novikov@desy.de

II. RESONANT X-RAY SCATTERING

Near absorption edges, anisotropic properties of resonant scattering lead to many interesting effects like various kinds of x-ray dichroism and appearance of forbidden reflections both in magnetic [39] and nonmagnetic [26,28] crystals. All these effects can be described in the frame of tensorial properties of absorption and the atomic scattering factor. The latter characterizes the resonant atomic scattering strength at x-ray energies close to absorption edges and is usually represented as a sum of several contributions [19]:

$$f_{jk} = f_0\delta_{jk} + f_{jk}^{\mathrm{dd}} + \mathrm{i}f_{jkn}^{\mathrm{dqs}}(k_n - k'_n) + \mathrm{i}f_{jkn}^{\mathrm{dqa}}(k_n + k'_n) + \ldots. \quad (1)$$

Here, f_0 describes the nonresonant contribution, f_{jk}^{dd} is the dipole-dipole contribution and $f_{ijk}^{\mathrm{s}} = \frac{1}{2}(f_{ijk} + f_{jik}^{*})$ and $f_{ijk}^{\mathrm{a}} = \frac{1}{2}(f_{ijk} - f_{jik}^{*})$ are the dipole-quadrupole contributions, which denote symmetric and antisymmetric parts, respectively, in terms of first and second index permutation. The value of the contribution decreases with increasing rank of the tensor. Furthermore, **k** and **k**′ are the wave vectors of the incident and scattered radiation, respectively.

For forbidden reflections, the nonresonant structure factor $F(\mathbf{H})$ equals zero. These purely resonant reflections can appear only in crystals of nonsymmorphic space groups, where glide planes and/or screw axes cause extinctions, which are removed due to the tensorial properties of the atomic scattering factor at energies close to an absorption edge [25,26]. Being a well-known ferroelectric with a Curie temperature of $T_c = 146$ K, RDP exhibits this kind of symmetries in both the ferroelectric and the paraelectric phase. In the ferroelectric phase, spontaneous electric polarization appears along the c axis and the structure can be described within the face-centered orthorhombic space group $Fdd2$ with a unit cell containing eight asymmetric units ($Z = 8$). In this case, Rb atoms are pairwise connected by an m_x glide plane with a translation vector $(0, \frac{1}{4}, \frac{1}{4})$, resulting in a set of extinctions [40]. Above the phase transition, the structure transforms into space group $I\bar{4}2d$ ($Z = 4$), where the Rb atoms lie on a fourfold rotoinversion axis on the $4b$ position and two Rb atoms are connected by a diagonal glide plane. For detailled crystallographic information, such as lattice parameters and atom positions, which we used for our calculations, see Ref. [4].

Below, we shall describe the experimental study of the $\{hhl \mid 2h + l = 4n + 2\}$ set of reflections, which are forbidden far from the Rb absorption edge both below and above the phase transition temperature. Here, we use the reflection indices corresponding to the tetragonal phase. However, below the phase transition the **a** and **b** basis vectors are rotated by 45° and twice as long, leading to a transformation of the reflection indices. The structure factor of these forbidden reflections is equal to

$$F(hhl, 2h + l = 4n + 2) \sim (f_1 - f_2), \quad (2)$$

where f_1 and f_2 are the tensorial scattering factors of the Rb atoms at positions $0,0,\frac{1}{2}$ and $\frac{1}{2},0,\frac{1}{4}$, connected by the diagonal glide plane. The site symmetry of Rb is $\bar{4}$, providing the transformations of coordinates: $x,y,z \to y,-x,-z \to -x,-y,z \to -y,x,-z$. In the ferroelectric phase, the reflections are allowed within the dipole-dipole approximation where the scattering factor of Rb is described by a uniaxial second-rank tensor. They are determined by only one tensor component which disappears in the paraelectric phase due to the fourfold symmetry of the Rb position. So, above the phase transition, this extinction can be removed only by higher order transitions or any other contribution to the atomic scattering factor, increasing its tensor rank as is described in Ref. [38]. Taking into account the third-rank part, the point group of the local position of Rb allows four tensor components [41]. Two of them ($f_{xxz} = -f_{yyz}$ and f_{xyz}) are symmetric over first two indices permutation, whereas the other two allow both symmetric and antisymmetric parts ($f_{yzy} = -f_{xzx}$ and $f_{yzx} = f_{xzy}$). The contribution to the structure factor comes from the components $f_{xxz} = -f_{yyz}$ and $f_{yzy} = -f_{xzx}$, which change their sign under the fourfold rotation. This way, it was shown that in the paraelectric phase the structure factor is described by the following tensor [38]:

$$F(hkl) \sim \begin{pmatrix} f_{xxz}^{\mathrm{s}}H_z & 0 & f_{xzx}^{\mathrm{s}}H_x + f_{xzx}^{\mathrm{a}}l_x \\ 0 & -f_{xxz}^{\mathrm{s}}H_z & f_{yzy}^{\mathrm{s}}H_y + f_{yzy}^{\mathrm{a}}l_y \\ f_{xzx}^{\mathrm{s}}H_x - f_{xzx}^{\mathrm{a}}l_x & f_{yzy}^{\mathrm{s}}H_y - f_{yzy}^{\mathrm{a}}l_y & 0 \end{pmatrix}, \quad (3)$$

where $H_k = k_k - k'_k$, $l_k = k_k + k'_k$.

The symmetric third-rank components may include three kinds of contributions: the intrinsic part caused by dipole-quadrupole transitions, a thermal motion induced part (TMI), which is proportional to the derivative of the dipole-dipole term over the resonant atoms thermal displacement and, last, contributions, which correspond to the transient proton configurations (PC). The latter can appear due to the deformation of the environment of the resonant atom associated with the transient configuration of hydrogen atoms. TMI as well as PC contributions cannot contain an antisymmetric part being proportional to the momentum transfer vector **H** and dipole-dipole in nature, and both are temperature dependent. The temperature dependence of the contributions to the forbidden reflections caused by dipole-dipole or dipole-quadrupole transitions is conventional, so their intensity decreases with temperature in accordance with the Debye-Waller factor. On the other hand, the TMI part grows with temperature and an anomalous temperature dependence of the forbidden reflection integrated intensity should be observed in the paraelectric phase. However, the intensity caused by dipole-dipole transitions is larger than that of the dipole-quadrupole and

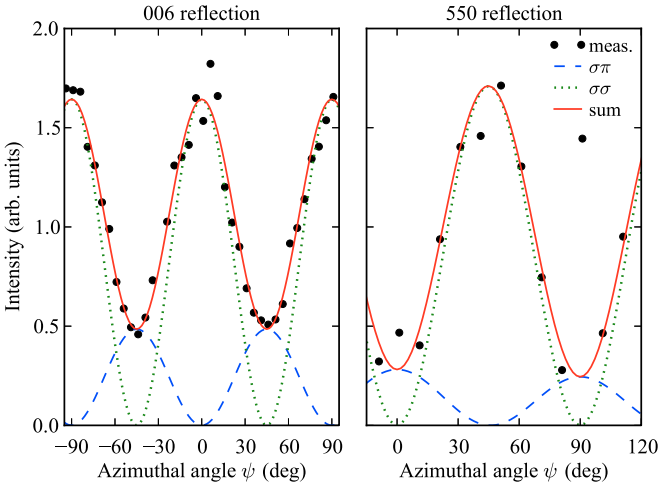

FIG. 1. (Color online) Measured azimuthal dependencies of the 006 (left) and 550 (right) forbidden reflections in the paraelectric phase at a photon energy of 15 196 eV (black dots). The curves calculated according to Eqs. (6) and (7) in Sec. IV A and Eqs. (8) and (9) in Sec. IV B for σ and π polarized scattered beams are shown as broken lines. The $\psi = 0$ azimuthal position refers to the situation where the scattering plane is parallel to the (100) lattice planes for the 006 reflection or rather to the (001) lattice planes for the 550 reflection. The measurement is described by the sum of both polarizations (solid red line).

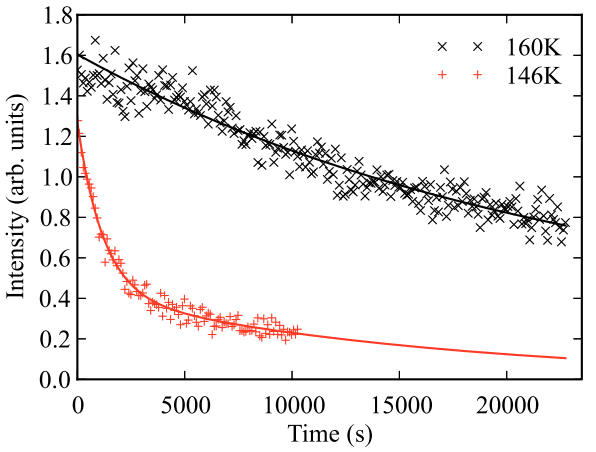

FIG. 2. (Color online) Degradation of the 550 reflection with time at different temperatures. Solid lines indicate the result of a biexponential fit that is used to correct for radiation damage effects.

higher-order terms and, therefore, we can expect an increase of the intensity of the reflections $\{hhl \mid 2h+l=4n+2\}$ when decreasing the temperature through the phase transition from para- to ferroelectric phase.

III. EXPERIMENTAL

The measurements were carried out at the resonant scattering undulator beamline P09 at PETRA III (DESY, Hamburg) [42] using a Si(111) double crystal monochromator and a pair of mirrors for focusing and higher harmonics rejection. Two RDP single crystals were grown in the Institute of Crystallography, Russian Academy of Sciences, and cut along (001) and (110) planes resulting in a size of approx. $7\times7\times2$ mm^2. They were mounted into the closed-cycle helium cryostat, which was installed at the Psi-diffractometer with open Chi-circle, present at the beamline. The incident photon beam was polarized perpendicular to the scattering plane. Optically, as well as by comparing rocking curves from different positions, the crystals appeared very homogeneous after polishing and the width of the rocking curve ($\approx 4''$) confirmed a good quality. Because all our considerations are done in kinematical approximation and based on the integrated intensity of the rocking curves, the mosaicity is not important.

A set of rocking curves was taken for the 006 and 550 forbidden reflections at energies near the K-absorption edge of Rb (15 200 eV) with a step width of 1 eV. The energy spectra were measured for different temperatures ranging from room temperature to below the phase transition temperature at 146 K. Temperature dependence of the lattice parameters as well as the thermal expansion of the setup were characterized beforehand to correct the positions of the Bragg reflections and the sample automatically.

Azimuthal dependencies of both reflections as shown in Fig. 1 were recorded at room temperature to choose positions near the maximum of the forbidden reflection intensity. There were two main difficulties complicating the experiment: the first was a big number of Renninger reflections due to the relatively high photon energy, the second was the fast degradation of the crystals under the powerful synchrotron beam. Figure 2 shows the time dependence of the 550 reflection intensity at two temperatures. One can see that the reflection degradation is stronger at lower temperature. During the measurements, we cooled the samples and heated them up to room temperature several times. Doing so, we observed healing of the crystals at higher temperatures, which suggests that two competing processes are taking place. A strong radiation damage of RDP under an intense x-ray beam was observed for the first time, but damage in KDP caused by powerful visible light was reported repeatedly [43,44]. To minimize its impact on the measured spectra of the forbidden reflections, the beam has slightly been defocused and attenuated such way that a compromise with respect to reasonable data acquisition time was found. Additionally, different position on the sample surface were used. The spectra have been obtained while cooling down as well as while warming up, whereas at temperatures near the phase transition (<160 K) only spectra recorded during heating appeared to be reliable.

In Fig. 3, an overview of integrated intensities of the rocking curves in dependence of incident photon energy as well as temperature is presented for the 006 forbidden reflection. Renninger reflections, visible as narrow maxima on sloping, near-horizontal lines, essentially impair the quality of many spectra. To prevent an influence of this effect, rocking curves where selected out of a set recorded at two or more azimuthal positions. Still, some spectra obviously were not reliable and, therefore, omitted. The remaining spectra for both reflections are presented in Fig. 4. Using these data, the intensity at the maximum position (15 196 eV) was selected for both 006 and 550 reflections and corrected for their time dependence caused by radiation damage. The temperature dependence

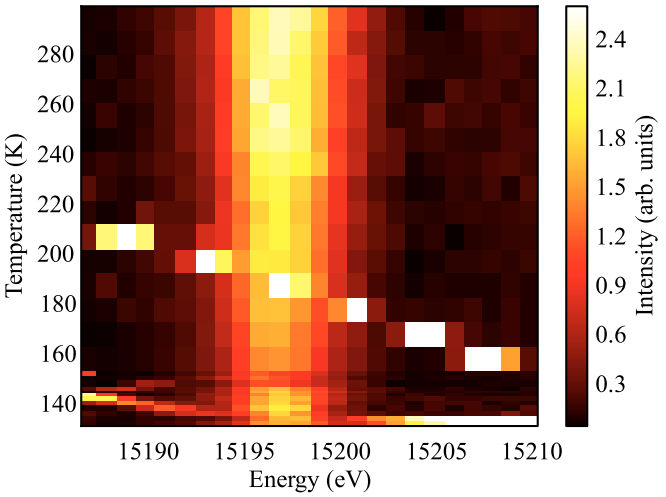

FIG. 3. (Color online) The dependence of integrated intensity of the 006 reflection on energy and temperature. The forbidden reflection is visible as maximum at constant energy (≈15 196 eV), whereas Renninger reflections occur at different energy for each temperature, since their position depends strongly on the lattice parameters.

thus obtained is shown in Fig. 5. In consideration of the conventional temperature dependence in x-ray diffraction, the integrated intensities are divided by the Debye-Waller factor taken from literature [4]. This way, the temperature dependencies of the purely resonant parts have been extracted for all spectra in Fig. 4.

Both reflections feature a decrease of integrated intensity with decreasing temperature in the paraelectric phase in accordance to the theoretical description of the TMI part of forbidden reflections. Further, a steplike increase of the intensity can be observed when cooling below the phase transition temperature, entering the ferroelectric phase. This enhancement is more pronounced in the case of the 006 reflection (see Fig. 5) but still about two orders of magnitude smaller than predicted by theory. One of the possible reasons is a complex domain structure in the sample and the resulting strain. Based on high resolution x-ray diffraction data of RDP, it has been concluded that, below T_c, ferroelastic strain in the (a,b) plane leads to micro-angle grain boundaries at the domain walls [7]. Additionally, the 550 reflection is split into two nearby reflections in the ferroelectric phase (10,0,0 and 0,10,0) that are allowed in dipole-dipole approximation.

An x-ray absorption spectrum of an RDP single crystal as shown in Fig. 6 was obtained in a previous measurement and used to find suitable modeling parameters for simulation of the resonant reflection spectra as described in the following.

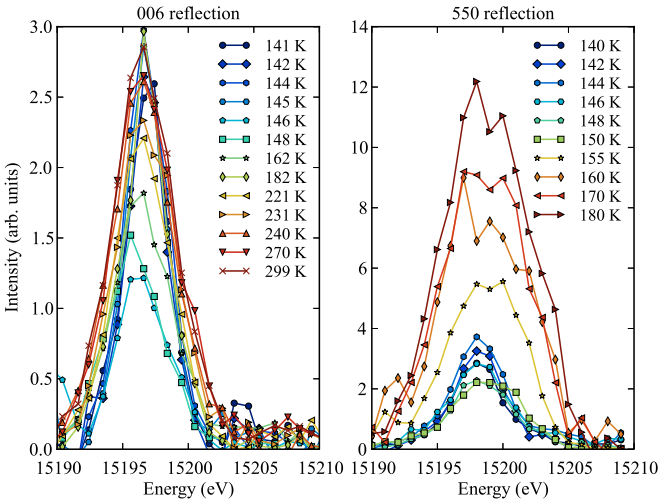

FIG. 4. (Color online) Energy spectra of the resonant reflections 006 (left) and 550 (right) at various temperatures showing that there is a minimum in intensity at about 148 K. The 550 reflection exhibits a higher energy width than the 006 reflection above the phase transition temperature.

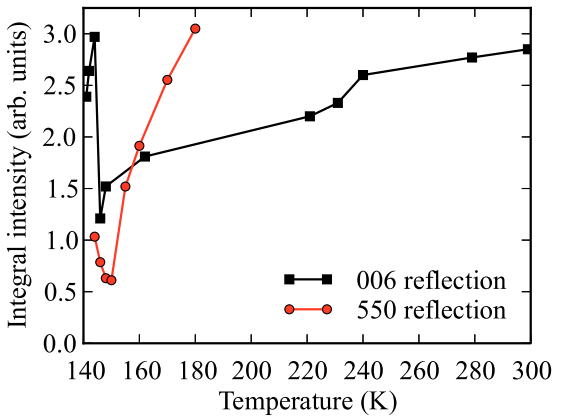

FIG. 5. (Color online) Temperature dependence of the intensities of the forbidden reflection integrated over energy, showing a stronger increase in case of the 550 reflection.

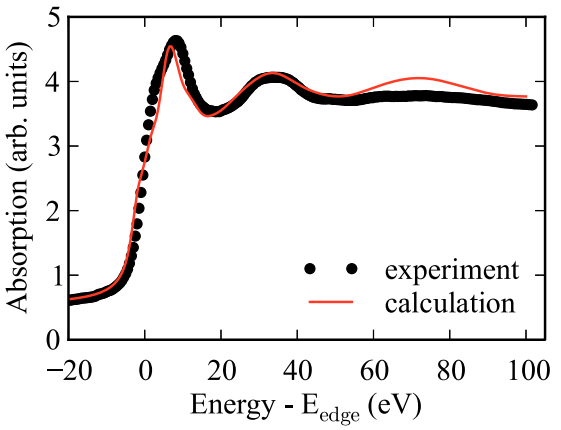

FIG. 6. (Color online) Absorption coefficient near the Rb K edge in RDP (experiment vs calculation within the model described in Sec. IV). The data have been used to correct the measured intensities and the calculation was performed to find suitable initial values for the simulation of the forbidden reflection spectra.

IV. MODELING OF FORBIDDEN REFLECTION ENERGY SPECTRA: PARAELECTRIC PHASE

In this section, the procedure to model the experimental results is described. Usually, the kinematical approximation of diffraction theory is believed to be valid for purely resonant x-ray scattering, whose amplitude is much less than in conventional x-ray diffraction. Then, the integrated intensity of the forbidden reflection can be written as [25,45]

$$I_{\mathbf{e}\mathbf{e}'}(\mathbf{H},E) \propto \mathrm{e}^{-2M} \frac{\mid e_i e'_j F_{ij}(E,\mathbf{H}) \mid^2}{\mu(E,\mathbf{e}) + \mu(E,\mathbf{e}')\, g}, \tag{4}$$

where e^{-2M} is the Debye-Waller factor, $\mu(E,\mathbf{e})$ is the linear absorption coefficient, dependent on the energy E and the polarization $\mathbf{e}$ or $\mathbf{e}'$ of the incident or scattered beam, respectively. The polarization can be reduced to the two cases of perpendicular (σ) and parallel (π) with respect to the scattering plane so that, in the present case of a σ-polarized incident beam, the measured intensity is a sum of: $I = I_{\sigma\sigma} + I_{\sigma\pi}$. The geometrical factor g is defined as $g = \frac{\sin\alpha}{\sin\beta}$, where α and β are respectively the angle of incidence and angle of reflection relative to the sample surface. In our cases, $g = 1$. As mentioned above, the resonant part of absorption depends on polarization in noncubic crystals [20], but this anisotropy is usually small [46] and will be neglected below. To model the resonant part of $\mu(E)$ numerically, we have used the FDMNES code [47–49]. The calculations were performed within the multiple scattering approximation and a cluster size of 7.5 Å. The arctangent model describing the energy dependence of the core hole width $\Gamma(E)$ was used for the convolution. The resulting fit is shown in Fig. 6. The parameters thus obtained form the basis for further simulations of the forbidden reflection spectra below.

Following the model proposed in Sec. II, the structure factor of the forbidden reflections is represented by Eq. (3). We assume each tensor component to be a sum of the dipole-quadrupole, TMI, and PC contributions. The first convolution was calculated using the FDMNES code and including the quadrupole-quadrupole part, though the latter turned out to be much smaller and, therefore, was neglected in the following.

The TMI contribution was calculated taking only the resonant atoms displacement into account. A detailed study of the TMI effect in Ge, ZnO, and GaN has shown that it is in fact provided by thermal displacements of atoms in several coordination spheres [35,50,51], but also that the main contribution arises from the displacement of the resonant atom itself. To obtain this component f^{TMI}_{xxz}, we displace the Rb atom from its average position by $0.001\,c$ along the z axis and calculate the derivative $\frac{\partial f^{\mathrm{dd}}_{xx}}{\partial z} = \frac{\Delta f^{\mathrm{dd}}_{xx}}{\Delta z}$. In analogous manner, we displace the Rb atom by $0.001\,a$ along the x axis and calculate $\frac{\partial f^{\mathrm{dd}}_{zx}}{\partial x} = \frac{\Delta f^{\mathrm{dd}}_{zx}}{\Delta x}$ to obtain the component f^{TMI}_{zxx}. Similar displacement along the y axis confirms $\frac{\partial f^{\mathrm{dd}}_{zy}}{\partial y} = -\frac{\partial f^{\mathrm{dd}}_{zx}}{\partial x}$ in accordance with the relation $f_{xzx} = -f_{yzy}$.

In the following, we describe the procedure used to calculate the contribution, which can appear due to the effect of hydrogen occupying only half of the crystallographical site [7]. The typical period of hydrogen transfer ($\sim 10^{-12}$ s) is much longer than that of x-ray resonant scattering ($\sim 10^{-15}$ s). Therefore an effect manifesting itself in a similar way, but different to the TMI in origin, can appear due to an additional contribution to the displacement of the resonant atom. In a certain case, the dipole-dipole components of the resonant atom may differ depending on which part of the hydrogen position is actually occupied in the moment of scattering. However, the structure factor will maintain the same symmetry after averaging over all possible configurations. Only if there is a correlation between the hydrogen configuration and a displacement $\mathbf{u}$ of the resonant atom, it can give rise to a contribution to the third-rank tensor components of the scattering factor which does not disappear after averaging. This effect stands in the focus of our investigations and will be referred to as PC (proton configurations) term in the following.

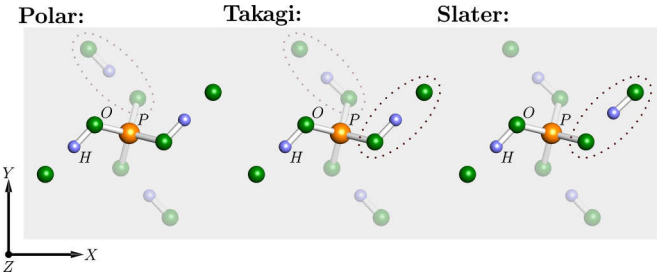

FIG. 7. (Color online) A cut of the unit cell of RDP with $\frac{1}{3} < z < \frac{2}{3}$ for each of the different proton configurations. The differences are highlighted. A semitransparent plane ($z = \frac{1}{2}$, containing P and Rb atoms) is drawn to illustrate the different z positions of the O-H groups. The shortest interatomic distances for both P-O and O-H are indicated by bonds.

To model the PC contributions to the structure factor we take into account several proton configurations, namely "Polar" (p), "Slater"(s), and "Takagi" (t), that are usually considered in the theory of hydrogen bonded crystals [9,10,16]. In case of "p" and "s" configurations, only two protons are attached to a PO_4 tetrahedron, which is known as the ice rule (see Fig. 7). In particular, p describes a configuration where two protons are attached to the opposite upper sides of the PO_4 group (providing the dipole moment along z axis), whereas in s configurations protons are attached to one "lower" and one "upper" side, which mainly causes a deformation of the environment in the xy plane. We also considered t configurations, where three protons are attached to one PO_4 group and one proton to the next group. *Ab initio* calculations have shown that the activation energy of t configurations is much higher than that of s or p [16]. Nevertheless, these configurations play an important role in the description of the phase transition [1,10].

For the simulation of PC contributions to the forbidden reflection structure factor, we constructed cells where all protons are situated in p, s, or t sites. In all cases, we can construct a pair of symmetrically equivalent p, s, or t configurations, where the sum of each pair statistically completely fills the crystallographic position of hydrogen, which is in reality only half-filled, as mentioned above. These configurations will be referred to as p_1, p_2, s_1, s_2, t_1, t_2 in

the following. For each of them, we calculated the Cartesian tensor components using the FDMNES code.

As a result, the dipole-dipole tensor components change differently with respect to the different proton configurations, so that

$$f_{ij}^{m}(C_n) = f_{ij}^{0} + \Delta f_{ij}^{m}(C_n).$$

Here, $m = 1,2$ denotes the two resonant atoms [see Eq. (2)], f_{ij}^{0} is a part equal for all configurations and $\Delta f_{ij}^{m}(C_n)$ is the correction corresponding to the configuration C_n, where C stands for the p, s, or t configuration and $n = 1,2$. Determined by symmetry, the following relations exist: $\Delta f_{ij}^{1}(C_1) = \Delta f_{ij}^{2}(C_2)$ and $\Delta f_{ij}^{1}(C_2) = \Delta f_{ij}^{2}(C_1)$. Using these and assuming equal probabilities P_n for both realizations of a specific configuration C, the structure factor

$$F_{ij}(\mathbf{H},C) = 2\sum_{m,n} P_n f_{ij}^{m}(C_n)\exp(\mathrm{i}\mathbf{H}\mathbf{r}^{m}) \tag{5}$$

becomes zero for the considered set of forbidden reflections. Thus, for each PC, we get the symmetry $F_{ij}(\mathbf{H},C_1) = -F(\mathbf{H},C_2)$. If we, however, take into account the structure relaxation of a certain proton configuration, it results in an additional displacement $\mathbf{r}^{m} = \mathbf{r}_0^{m} + \mathbf{u}^{m}(C_n)$ and hence the following term appears in the structure factor [38]:

$$\begin{aligned}\Delta F_{ij}(\mathbf{H},C) &= \sum_{n} P_n \Delta F_{ij}(\mathbf{H},C_n)\\ &= 2\mathrm{i}\sum_{k,m,n} P_n f_{ijk}^{m}(C_n) H_k \exp(\mathrm{i}\mathbf{H}\mathbf{r}_0^{m}),\end{aligned}$$

where $f_{ijk}^{m}(C_n) = \Delta f_{ij}(C_n) u_k^{m}(C_n)$.

Using the *ab initio* code VASP [52,53], we modeled the relaxation of all atomic sites in the presence of each of the proton configurations and afterwards again calculated the cartesian dipole-dipole tensor components of the scattering factors with the help of the FDMNES code. We find that (1) in the relaxed lattice, the difference between the Cartesian components of the p_1 and p_2, s_1 and s_2, t_1 and t_2 is higher than in unrelaxed lattice by several percents. This difference well exceeds the calculation error caused by the limited number of atoms involved in the multiple scattering process. (2) Polar configurations lead to an opposite Rb atom displacement along the z axis for p_1 and p_2. As a result, only the tensor components $f_{xxz}(p_n) = -f_{yyz}(p_n)$ exist and provide a contribution to the structure factor: $\Delta F_{xx}(\mathbf{H},p_n) = -\Delta F_{yy}(\mathbf{H},p_n)$. (3) Slater configurations result in an Rb displacement mainly in the xy plane, so that the tensor components $f_{xzx}(s_n) = -f_{yzy}(s_n)$ contribute to the structure factor: $\Delta F_{xz}(\mathbf{H},s_n) = -\Delta F_{yz}(\mathbf{H},s_n)$. (4) Takagi configurations provide the contributions to all listed structure tensor components. However, the activation energy of such configurations is higher than the others, so their probability is small, which is why they were neglected.

Figure 8 shows the square modulus of the dipole-quadrupole, TMI, and PC (including "polar" and "slater") contributions to the structure factors of the 006 and 550 reflections. All contributions are scaled aiming to see their shape and the position in energy. A temperature dependence of the PC contribution to the scattering factor of the forbidden reflections may exist because the number of the various configurations changes with temperature.

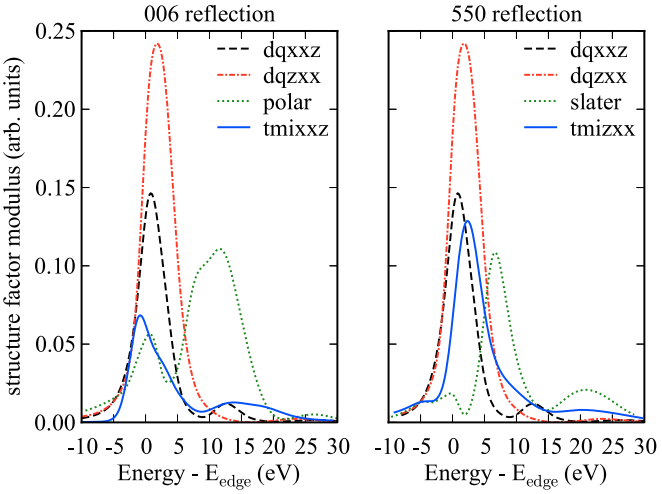

FIG. 8. (Color online) Various contributions to the 006 (left) and 550 (right) forbidden reflection structure factor. It can be seen that proton configurations cause characteristic spectra with shifted maxima positions allowing to distinguish them from other contributions. They are scaled for better visibility.

A. Fitting of the 006 reflection energy spectra

The resonant scattering amplitudes for the 006 forbidden reflection has the following form:

$$F_{\sigma\sigma}(006) = 4k\sin\theta_{\mathrm{B}} f_{xxz}^{\mathrm{s}}\cos 2\phi, \tag{6}$$

$$F_{\sigma\pi}(006) = 4k\sin 2\phi\left(\sin^2\theta_B f_{xxz}^{\mathrm{s}} - \cos^2\theta_B f_{xzx}^{\mathrm{a}}\right), \tag{7}$$

where ϕ is the azimuthal angle and θ_{B} the Bragg angle. We suppose that the scattering tensor component consists of

$$f_{xxz} = f_{xxz}^{\mathrm{dq}} + a_1(T) f_{xxz}^{\mathrm{TMI}} + a_2(T) f_{xxz}^{\mathrm{polar}},$$

where all components were calculated in the previous section and $a_i(T)$ are the variation parameters depending on temperature. The antisymmetric part of the tensor is provided only by the dipole-quadrupole term and equal to $f_{xzx}^{\mathrm{a}} = \frac{1}{2}(f_{xzx}^{dq} - f_{zxx}^{dq*})$. The PC contributions for this reflection can only be caused by polar hydrogen configurations. Figure 1 (left panel) shows the azimuthal dependence of the 006 reflection for the paraelectric phase, calculated for the dipole-quadrupole term as shown in Eqs. (6) and (7). One can see that the experimental azimuthal dependence fits the calculated one.

The expression (4) together with (6) and (7) were applied for fitting the 006 reflection energy spectra at the azimuthal angle used in the experiment (45°, maximum of intensity). As can be seen in Fig. 8 (left panel), the dipole-quadrupole and TMI terms f_{xxz} peak approximately at the same energies, whereas the polar PC term is shifted to higher energies. The measured spectra look similar for all temperatures. Only their intensity grows with temperature. Thus, we conclude that the spectra of the 006 reflection can be fitted using only the dipole-quadrupole and TMI terms. The presence of the polar PC term is not obvious, which means that the corresponding tensor component is small and more detailed measurements might be necessary to resolve it. Figure 9 shows the results of fitting

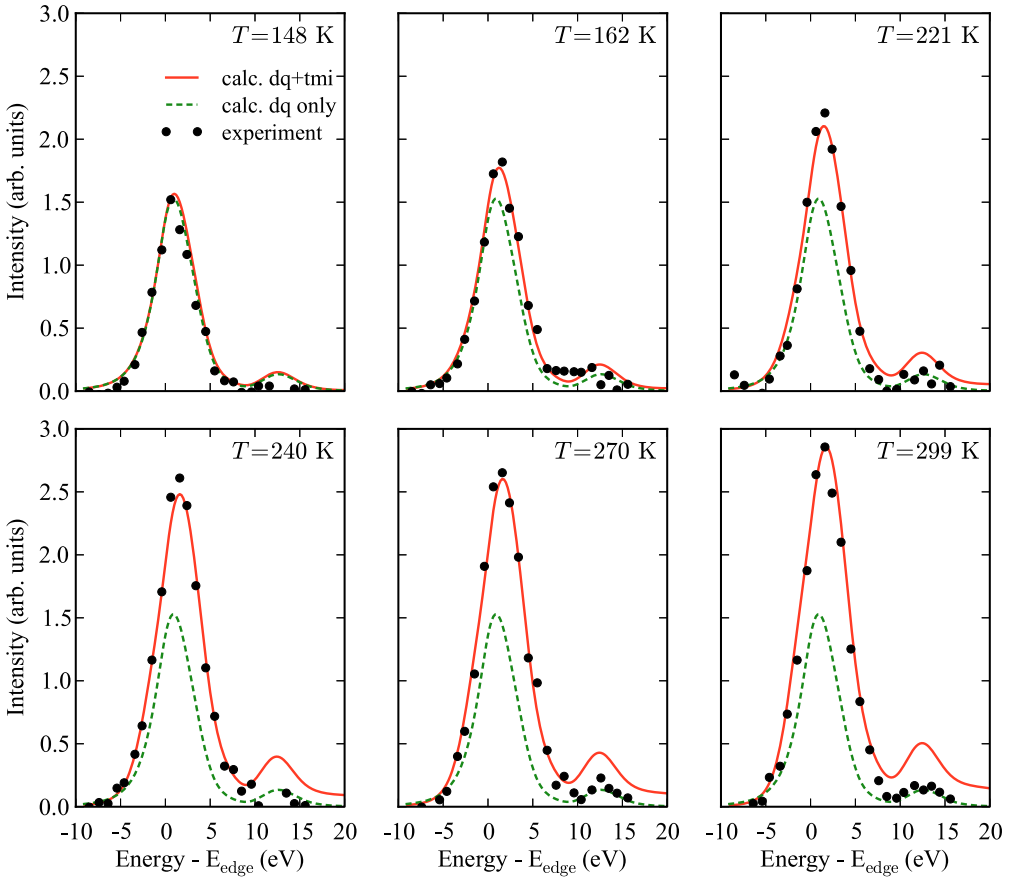

FIG. 9. (Color online) Energy spectra of the 006 reflection at chosen temperatures (experiment vs calculation) showing that they can be described by taking into account intrinsic dipole-quadrupole and TMI contribution only.

the 006 forbidden reflection energy spectra for a set of chosen temperatures in comparison with experimental data.

It would be interesting to compare the obtained temperature dependence of the 006 reflection with a similar dependence of the 006 reflection in Ge [35]. In both cases, the shape of the energy spectra is simple and does not essentially vary with temperature. The temperature dependence of the 006 reflection intensity in the Ge case approximately shows a parabolic behavior $I \sim T^2$. An easy explanation for this dependence in Ge was that there is only one low lying optical vibration mode, which gives contribution to the TMI effect leading to $\bar{u}^2 \sim T$ at high temperatures. In RDP, the experimental temperature dependence is not monotonic, but at high temperatures it is close to a linear function.

In KDP, there are 45 optical modes present [54]. Owing to the similarity between the RDP and KDP structures, the number of optical modes in RDP also might be large and we cannot tell which contribution prevails.

B. Fitting of the 550 reflection energy spectra

The scattering amplitudes for the 550 reflection has the following form:

$$F_{\sigma\sigma} = 4k \sin 2\phi \sin\theta_B f^s_{zxx}, \quad (8)$$

$$F_{\sigma\pi} = 4k\big(-f^s_{zxx} \sin^2\theta_B \cos 2\phi + f^a_{zxx} \sin^2\phi \cos^2\theta_B\big), \quad (9)$$

with $f_{zxx} = f^{dq}_{zxx} + b_1(T) f^{TMI}_{zxx} + b_2(T) f^{slater}_{zxx}$. TMI and PC terms do not contain an antisymmetric part. The calculations are made for the azimuthal angle used in the experiment. In Fig. 8, one can see that for this reflection, the PC term is shifted to higher and the TMI is slightly shifted to lower energies with respect to the dipole-quadrupole term. Figure 10 shows the measured spectra for the 550 reflection and the corresponding fit of the spectra resulting from the discussed contributions. At high temperatures, the increase of the 550 integrated intensity with temperature is almost linear, similar to the 006 reflection. This can, in principle, be explained by the TMI mechanism, but the width of the simulated spectra for temperatures between 160 and 180 K is much lower than that in the experimental curves, as can be seen in Fig. 10. This discrepancy can be explained by the influence of the PC s term, which leads to a good agreement in shape and width of the spectra.

The coefficients a_1, b_1, and b_2 used for the fitting of the 006 and 550 forbidden reflection energy spectra are presented in Fig. 11. Certainly, only the relative values are shown. The experimental data and calculations cannot give the absolute value of these coefficients since a known reference is missing. Nevertheless, it is obvious that the thermal growth of the forbidden reflection intensity is mainly provided by the TMI mechanism, but including the PC contribution for the 550 reflection considerably improves the fit of the simulations.

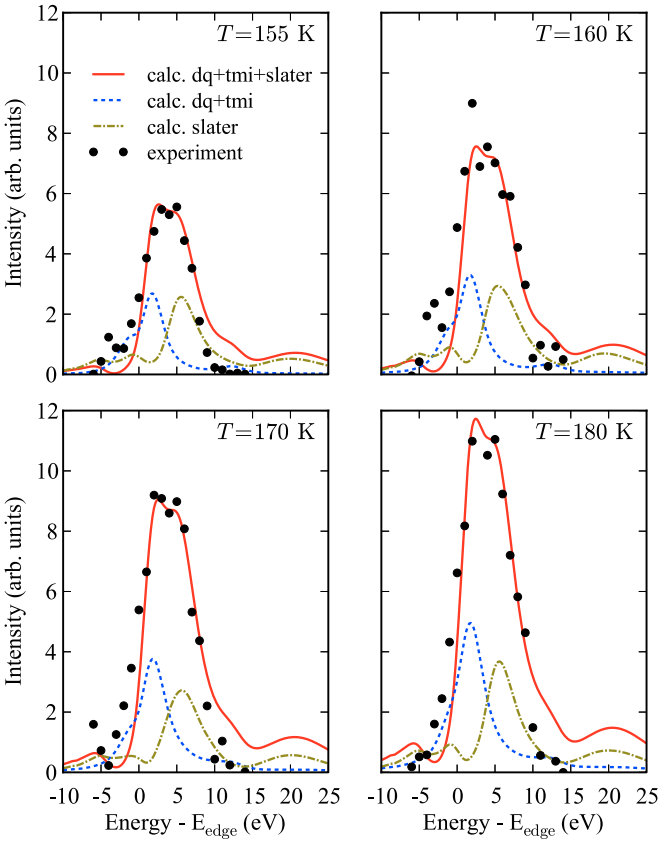

FIG. 10. (Color online) Energy spectra of the 550 reflection (experiment vs calculation). The total intensity is proportional to the square modulus of the sum over the amplitudes of all contributions. As a reference, the intensities of isolated contributions are shown as broken lines. "Slater"-type proton configurations had to be taken into account to be able to model the measured spectra.

V. CONCLUSIONS

In the present paper, the proton ordering in a KDP-isomorphous kind of hydrogen-bonded ferroelectrics was studied with resonant x-ray diffraction. The observed effects depend on the complexity of the transient environment of the resonant atom and the resulting influence on the atomic scattering factor at energies close to absorption edges. Being averaged over the observation time, the time dependent resonant structure factor does not turn to zero and leads to the appearance of the TMI contribution to forbidden reflections associated with thermal vibrations.

In rubidium dihydrogen phosphate, protons participate in one more kind of movement, namely tunneling between two close crystallographic sites. This provides an additional contribution to the resonant atomic scattering factor, whose temperature dependence is caused by the variation of proton configurations around the resonant atom. This variation is one of the reasons leading to the phase transition, because all protons occupy the polar sites in the ferroelectric phase. The observed temperature dependence of the forbidden reflections, in particular the enhancement of the 006 forbidden reflection intensity, can be successfully explained by a thermal motion induced contribution consistent with the adiabatic approximation stating that electrons follow the movement of the nuclei.

In the frame of the developed theoretical model, it was shown that the change of the intensity and the energy spectrum of the 550 forbidden reflection can only be explained by taking into account one more contribution to the resonant structure factor corresponding to slater-type proton configurations. Furthermore, an increase of the number of these configurations with temperature has been observed. A quantitative analysis of this effect was complicated by structural changes in the RDP crystals, which were associated with interaction of the sample and the intense x-ray beam and proved to be temperature dependent.

Our research has demonstrated high sensitivity of the forbidden reflection energy spectra to the local environment of the resonant atoms and structural changes of the crystal, which makes this method very promising for the study of phase transitions and other processes accompanied by atomic displacements and ordering.

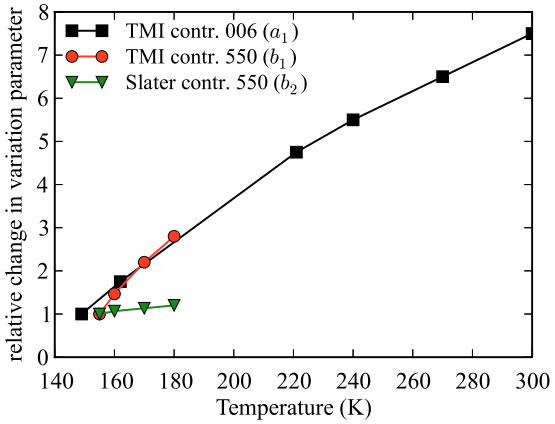

FIG. 11. (Color online) Relative change in the variation parameters (a_1,b_1,b_2) with temperature for 006 and 550 reflections. These represent the different contributions to the resonant scattering amplitude as defined in Secs. IV A and IV B.

ACKNOWLEDGMENTS

The research was done at the PETRA III Resonant x-ray scattering (RXS) beamline at DESY, a member of the Helmholtz Association (HGF). The authors acknowledge the support of the PETRA III staff for the RXS measurements. Part of this work was supported by BMBF Proposal No. 05100051 "Investigation of phase transitions with Resonant x-ray scattering" in the framework of the German-Russian collaboration "Development and use of accelerator-based photon sources." We also acknowledge financial support by the BMBF within project 05K10OF1 and by Grant RFBR 13-02-00760. The calculations have been performed using the *ab initio* total-energy and molecular-dynamics program VASP (Vienna *ab initio* simulation program) developed at the Institut für Materialphysik of the Universität Wien. The Moscow State University supercomputer SKIF was used for calculations.

[1] F. Jona and G. Shirane, *Ferroelectric Crystals* (Dover, New York, 1993).

[2] P. Bartschi, B. Matthias, W. Merz, and P. Scherrer, Helv. Phys. Acta **18**, 240 (1945).

[3] A. R. Al-Karaghouli, B. Abdul-Wahab, E. Ajaj, and A. Sequeira, Acta Crystallogr., Sect. B: Struct. Crystallogr. Cryst. Chem. **34**, 1040 (1978).

[4] N. Kennedy and R. Nelmes, J. Phys. C **13**, 4841 (1980).

[5] M. Averbuch-Pouchot and A. Durif, Acta Crystallogr., Sect. C: Cryst. Struct. Commun. **41**, 665 (1985).

[6] J.-H. Park, K.-S. Lee, and B.-C. Choi, J. Phys.: Condens. Matter **13**, 9411 (2001).

[7] S. Mattauch, G. Heger, and K. H. Michel, Cryst. Res. Technol. **39**, 1027 (2004).

[8] C. E. Botez, H. Martinez, R. J. Tackett, R. R. Chianelli, J. Zhang, and Y. Zhao, J. Phys.: Condens. Matter **21**, 325401 (2009).

[9] J. C. Slater, J. Chem. Phys. **9**, 16 (1941).

[10] Y. Takagi, J. Phys. Soc. Japan **3**, 271 (1948).

[11] R. Blinc, J. Phys. Chem. Solids **13**, 204 (1960).

[12] K. Kobayashi, J. Phys. Soc. Japan **24**, 497 (1968).

[13] R. Nelmes, J. Phys. C **21**, L881 (1988).

[14] H. Sugimoto and S. Ikeda, J. Phys.: Condens. Matter **8**, 603 (1996).

[15] S. Koval, J. Kohanoff, J. Lasave, G. Colizzi, and R. L. Migoni, Phys. Rev. B **71**, 184102 (2005).

[16] J. Lasave, S. Koval, N. S. Dalal, and R. Migoni, Phys. Rev. B **72**, 104104 (2005).

[17] J. P. Hannon, G. T. Trammell, M. Blume, and D. Gibbs, Phys. Rev. Lett. **61**, 1245 (1988).

[18] S. W. Lovesey and S. P. Collins, *X-Ray Scattering and Absorption by Magnetic Materials* (Clarendon Press, Oxford, 1996).

[19] M. Blume, *Resonant Anomalous X-Ray Scattering: Theory and Applications* (North-Holland, Amsterdam, 1994), Chap. Magnetic effects in anomalous dispersion.

[20] C. Brouder, J. Phys.: Condens. Matter **2**, 701 (1990).

[21] J.-L. Hodeau, V. Favre-Nicolin, S. Bos, H. Renevier, E. Lorenzo, and J.-F. Berar, Chem. Rev. **101**, 1843 (2001).

[22] S. W. Lovesey, E. Balcar, K. Knight, and J. Fernández Rodríguez, Phys. Rep. **411**, 233 (2005).

[23] V. E. Dmitrienko, K. Ishida, A. Kirfel, and E. N. Ovchinnikova, Acta Crystallogr., Sect. A: Found. Crystallogr. **61**, 481 (2005).

[24] S. Collins, S. Lovesey, and E. Balcar, J. Phys.: Condens. Matter **19**, 213201 (2007).

[25] V. A. Belyakov and V. E. Dmitrienko, Physics-Uspekhi **32**, 697 (1989).

[26] V. Dmitrienko, Acta Crystallogr., Sect. A: Found. Crystallogr. **39**, 29 (1983).

[27] V. Dmitrienko, Acta Crystallogr., Sect. A: Found. Crystallogr. **40**, 89 (1984).

[28] D. Templeton and L. Templeton, Acta Crystallogr., Sect. A: Found. Crystallogr. **41**, 133 (1985).

[29] D. H. Templeton and L. K. Templeton, Phys. Rev. B **49**, 14850 (1994).

[30] P. Carra and B. Thole, Rev. Mod. Phys. **66**, 1509 (1994).

[31] K. D. Finkelstein, Q. Shen, and S. Shastri, Phys. Rev. Lett. **69**, 1612 (1992).

[32] V. Dmitrienko, E. Ovchinnikova, and K. Ishida, J. Exp. Theor. Phys. Lett. **69**, 938 (1999).

[33] V. Dmitrienko and E. Ovchinnikova, Acta Crystallogr., Sect. A: Found. Crystallogr. **56**, 340 (2000).

[34] J. Kokubun, M. Kanazawa, K. Ishida, and V. E. Dmitrienko, Phys. Rev. B **64**, 073203 (2001).

[35] A. Kirfel, J. Grybos, and V. E. Dmitrienko, Phys. Rev. B **66**, 165202 (2002).

[36] S. P. Collins, D. Laundy, V. E. Dmitrienko, D. Mannix, and P. Thompson, Phys. Rev. B **68**, 064110 (2003).

[37] G. Beutier, S. Collins, G. Nisbet, E. Ovchinnikova, and V. Dmitrienko, Eur. Phys. J. Spec. Topics **208**, 53 (2012).

[38] E. K. Mukhamedzhanov, M. Kovalchuk, M. Borisov, E. Ovchinnikova, E. Troshkov, and V. Dmitrienko, Crystallogr. Rep. **55**, 174 (2010).

[39] D. Gibbs, D. Moncton, and K. DAmico, J. Appl. Phys. **57**, 3619 (1985).

[40] T. Hahn, U. Shmueli, A. A. J. C. Wilson, and E. Prince, *International Tables for Crystallography* (D. Reidel Publishing Company, 2005).

[41] S. Yu and M. P. Shaskolskaya, *Fundamentals of Crystal Physics* (Mir Publ, Moscow, 1982).

[42] J. Strempfer, S. Francoual, D. Reuther, D. K. Shukla, A. Skaugen, H. Schulte-Schrepping, T. Kracht, and H. Franz, J. Synchrotron Radiat. **20**, 541 (2013).

[43] R. Terhune, P. Maker, and C. Savage, Appl. Phys. Lett. **2**, 54 (1963).

[44] S. A. Akhmanov, A. I. Kovrigin, A. S. Piskarskas, V. V. Fadeev, R. V. Khokhlov, Sov. J. Exp. Theor. Phys. Lett. **2**, 191 (1965).

[45] R. W. James, *The Optical Principles of the Diffraction of X-Rays* (Ox Bow Press, Woodbridge (Connecticut), 1982).

[46] G. Beutier, E. Ovchinnikova, S. Collins, V.-E. Dmitrienko, J.-E. Lorenzo, J.-L. Hodeau, A. Kirfel, Y. Joly, A. Antonenko, V. Sarkisyan, *et al.*, J. Phys.: Condens. Matter **21**, 265402 (2009).

[47] Y. Joly, Phys. Rev. B **63**, 125120 (2001).

[48] O. Bunău and Y. Joly, J. Phys.: Condens. Matter **21**, 345501 (2009).

[49] Y. Joly, *The* FDMNES *project* (2012), URL http://neel.cnrs.fr/.

[50] E. Ovchinnikova, V. Dmitrienko, A. Oreshko, G. Beutier, and S. Collins, J. Phys.: Condens. Matter **22**, 355404 (2010).

[51] A. Oreshko, E. Ovchinnikova, G. Beutier, S. Collins, G. Nisbet, A. Kolchinskaya, and V. Dmitrienko, J. Phys.: Condens. Matter **24**, 245403 (2012).

[52] G. Kresse and J. Furthmüller, Phys. Rev. B **54**, 11169 (1996).

[53] G. Kresse and D. Joubert, Phys. Rev. B **59**, 1758 (1999).

[54] G. Lu, C. Li, W. Wang, Z. Wang, J. Guan, and H. Xia, Mater. Sci. Eng., B **116**, 47 (2005).